Chemical Science

ROYAL SOCIETY OF CHEMISTRY

EDGE ARTICLE

View Article Online
View Journal | View Issue

Cite this: *Chem. Sci.*, 2026, **17**, 8251

All publication charges for this article have been paid for by the Royal Society of Chemistry

Polarization-induced reversible electron–hole migration and redox reaction switching in ferroelectric single-atom photocatalysts

Yuan Tang,[a] Cen-Feng Fu,*[b] Xingxing Li *[c] and Jinlong Yang [c]

Received 4th December 2025
Accepted 26th February 2026

DOI: 10.1039/d5sc09491g

rsc.li/chemical-science

Photocatalysts capable of switching between oxidation and reduction reactions at a single active site can efficiently harness solar energy to selectively generate target products on demand, and are thus eagerly pursued. However, realizing such photocatalysts is quite challenging due to the difficulty in simultaneously accumulating both types of carriers at a single site and meeting the stringent requirements for electron–hole separation. Here, we propose that the switchable out-of-plane polarization of two-dimensional ferroelectric materials can reversibly steer either photogenerated electrons or holes to single active sites, and further enable controllable switching of photocatalytic oxidation and reduction. The first-principles calculations and nonadiabatic molecular dynamics simulations, performed on a photocatalyst comprising a Pd single-atom anchored on a ferroelectric Sc_2CO_2 monolayer, validate this strategy. Reversing the ferroelectric polarization direction in Sc_2CO_2 modulates carrier migration: an upward polarization state induces ultrafast hole accumulation at the Pd site (τ = 0.05 ps), whereas a downward polarization state drives rapid electron transfer to the Pd site (τ = 0.31 ps). Moreover, the Pd site exhibits low hydrogen and oxygen evolution reaction overpotentials (0.08 V and 0.29 V), enabling efficient overall water splitting. The proposed strategy establishes a novel avenue for precisely controlled photochemical synthesis at single active sites.

Introduction

Photocatalytic chemical reactions offer a promising route for converting solar energy into chemical energy.[1–6] In conventional photocatalysts, active sites are generally limited to driving either reduction or oxidation reactions. However, in certain cases, it is highly desirable to simultaneously produce diverse products or dynamically switch between specific products on demand. Bifunctional catalysts partially address this need. For instance, a bifunctional photocatalytic system used in value-added organic transformation can eliminate sacrificial reagents, significantly improving process economics.[7] Furthermore, such catalysts enhance the efficiency of energy utilization, enable tailored chemical synthesis, and reduce equipment modification costs.[8] Bifunctional catalysts are also essential for energy storage and conversion systems employing reversible oxygen electrodes, where both the oxygen evolution reaction (OER) and oxygen reduction reaction (ORR) must occur efficiently at the same electrode.[9] However, achieving bifunctional photocatalysts where a single active site can dynamically switch between driving reduction and oxidation reactions remains largely unexplored. This capability requires meeting three fundamental criteria: first, the photogenerated carriers (electrons and holes) should readily migrate to the active site. Second, the active site should catalytically drive the desired reactions using these carriers. Last, the dominant type of carrier (electron or hole) migrating to the active site should be reversibly controllable. Currently explored photocatalytic materials, including transition metal oxides/carbides/nitrides (MXenes),[10–12] Janus materials,[13] and organic polymers,[14] largely fail to satisfy all these conditions simultaneously. In a conventional photocatalyst, a single active site typically facilitates only one type of reaction: either oxidation or reduction. This limitation arises from two primary factors. One factor is that oxidation requires holes while reduction requires electrons; attempting both reactions at the same site promotes rapid carrier recombination. The other factor is that the inherent electronic and chemical properties of an active site usually favor the accumulation of only one type of carrier (electrons or holes), making controlled modulation of carrier migration exceptionally difficult.

Fortunately, two-dimensional (2D) ferroelectric (FE) materials provide a promising strategy for modulating the migration of photogenerated carriers. Their out-of-plane polarization

[a]*Hefei National Laboratory, School of Emerging Technology, University of Science and Technology of China, Hefei, Anhui 230026, China*

[b]*School of Materials Science and Engineering, Hefei University of Technology, Hefei, Anhui 230009, China. E-mail: cffu@hfut.edu.cn*

[c]*Hefei National Laboratory, State Key Laboratory of Precision and Intelligent Chemistry, University of Science and Technology of China, Hefei, Anhui 230026, China. E-mail: lixx@ustc.edu.cn*

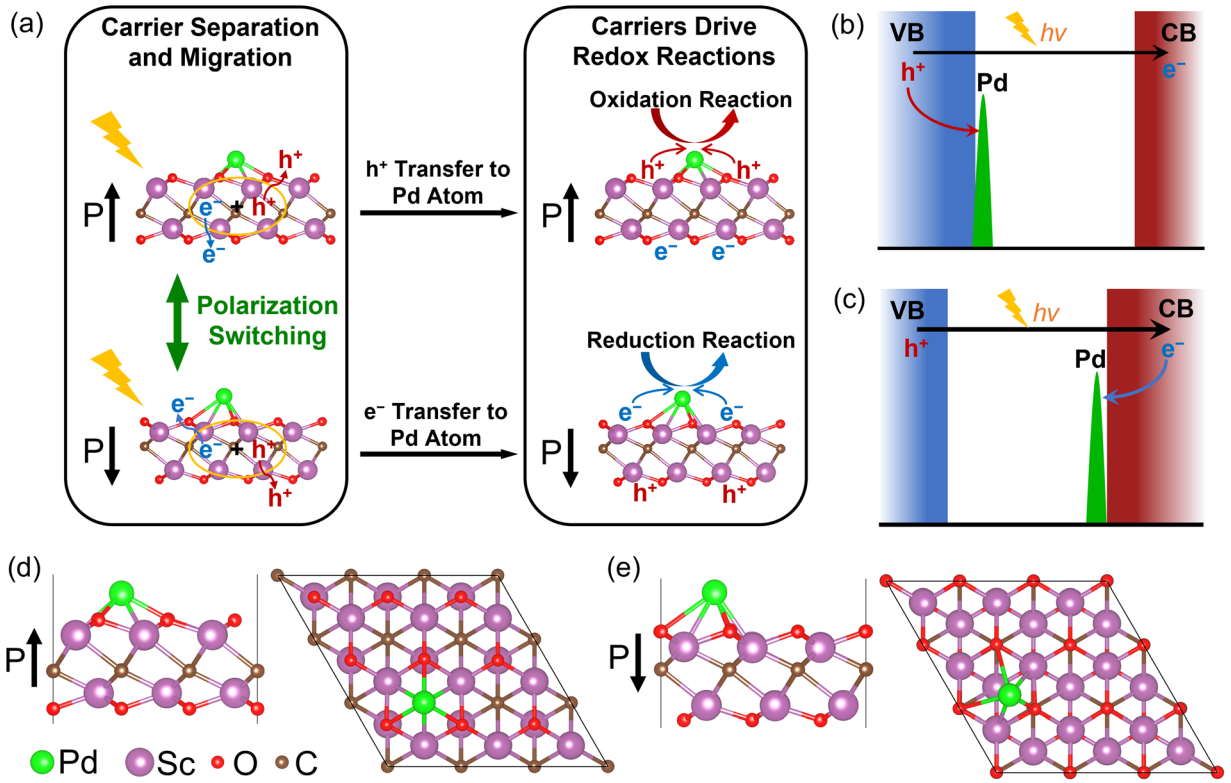

Fig. 1 (a) Schematic diagram of polarization-induced reversible electron–hole migration and redox reaction switching. The polarization directions for the out-of-plane ferroelectricity of Sc_2CO_2 are represented by the black arrows. (b) and (c) schematic diagram of electronic structures for photogenerated holes and electrons, respectively, migrating from Sc_2CO_2 to a Pd single-atom. (d) and (e) side view (left) and top view (right) of a Pd atom anchored on the upper surface of Sc_2CO_2 with upward and downward polarization directions, respectively.

creates a built-in electric field that effectively separates and directs photogenerated electrons and holes toward opposite surfaces.[15–22] This inherent capability has been leveraged in various photo-electrocatalytic systems to switch the photocatalytic process to an electrocatalytic process,[23] modify the capability to drive photocatalytic water splitting,[24] tune the selectivity for the carbon dioxide reduction reaction,[25] and optimize the activity of electrocatalytic water oxidation.[26] Despite these advances, in two-dimensional FE materials such as $AgBiP_2Se_6$,[24] the catalytic sites responsible for driving redox reactions are spatially partitioned onto opposing surfaces. This geometric separation establishes distinct domains for oxidation and reduction reactions, thereby preventing the same active site from switching between oxidative and reductive roles. Furthermore, previous investigations into ferroelectric photocatalysts have largely centered on the reaction pathways and thermodynamic characteristics of surface reactions, while often neglecting the carrier migration dynamics integral to photocatalytic processes. Hence, the fundamental influence of 2D FE polarization on carrier dynamics, particularly the underlying mechanisms governing electron–hole separation and migration, has not been well understood yet. On the other hand, while several 2D FE materials (*e.g.*, $Ti_3C_2T_x$,[27] Sc_2CO_2,[28] In_2Se_3,[29] $CuInP_2S_6$,[30] $AgBiP_2Se_6$,[24]) have been identified theoretically and experimentally, their pristine surfaces typically lack well-defined, catalytically active sites. This limitation highlights the potential of single-atom catalysts (SACs)[25] anchored on 2D FE substrates.[31–35] Integrating highly active, isolated metal atoms with the switchable polarization field of 2D FE materials presents a robust platform for achieving a dynamically switchable and bifunctional photocatalytic system at a single active site.

Building upon the synergistic potential of SACs and 2D FE materials, we conceptually propose a promising route to achieve controllable switching between driving oxidation and reduction reactions at a single active site of photocatalysts by incorporating a single-atom site onto 2D materials with out-of-plane ferroelectricity (Fig. 1). Leveraging the reversible out-of-plane polarization of the FE substrate, migration of photogenerated electrons or holes to the anchored single-atom site can be dynamically controlled. In detail, single-atom anchoring creates distinct intermediate states within the band gap of the substrate: one polarization leads to an occupied single-atom state near the valence band maximum, facilitating ultrafast hole capture, while the other polarization results in an empty single-atom state near the conduction band minimum, enabling rapid electron capture. Consequently, the single-atom site can alternately drive oxidation and reduction reactions depending on the polarization state of the FE substrate, with the help of corresponding photogenerated carriers. Through first-principles calculations and nonadiabatic molecular dynamics (NAMD) simulations, this strategy is validated on

a photocatalyst comprising a Pd single-atom anchored on the surface of a Sc_2CO_2 monolayer, a representative 2D MXene[36–40] with out-of-plane ferroelectricity.[28] The results demonstrate that polarization switching governs the selectively dynamic transfer of either photogenerated electrons or holes to the single active site. Furthermore, the designed photocatalyst is confirmed to be a high-activity single-atom photocatalyst for overall water splitting.

Results

To screen out switchable 2D FE single-atom photocatalysts, a series of candidate systems were evaluated based on two criteria: (1) the substrate material must exhibit robust out-of-plane FE polarization to modulate the intermediate states of the adsorbed single atom, along with an appropriate band gap to drive the desired redox reactions. (2) upon single-atom adsorption, switching the direction of FE polarization should enable modulation of the intermediate state potentials, thereby allowing the single atom to selectively accept either photogenerated electrons or holes, respectively. Among the FE materials, Sc_2CO_2 (a MXene derivative) was selected as a representative model system due to its robust out-of-plane FE polarization and suitable band edge alignment. Then, a range of transition metal atoms spanning the 3d, 4d, and 5d series were screened for anchoring onto the Sc_2CO_2 surface. The results revealed that only the Pd@Sc_2CO_2 system satisfied both core requirements. Eventually, the FE photocatalyst composed of a Pd single-atom supported on the surface of Sc_2CO_2 (denoted as Pd@Sc_2CO_2) is taken as a typical model to validate the proposed strategy. As a 2D monolayer with out-of-plane ferroelectricity, Sc_2CO_2 exhibits reversible polarization switching between upward and downward directions,[28] thereby dynamically regulating the migration of photogenerated electrons and holes to the two different surfaces (Fig. 1a). When the polarization direction of Sc_2CO_2 is upward (denoted as $Sc_2CO_2\uparrow$), photogenerated holes are concentrated on the upper surface, while photogenerated electrons accumulate on the lower surface. Conversely, when the polarization direction is downward (denoted as $Sc_2CO_2\downarrow$), photogenerated holes and electrons are enriched on the lower and upper surfaces, respectively, effectively reversing their distribution compared to $Sc_2CO_2\uparrow$. Therefore, flipping the polarization direction dynamically controls either holes or electrons concentrated on the upper surface of Sc_2CO_2. Fig. 1d and e present the optimized geometric structures of a Pd single-atom anchored on the upper surface of $Sc_2CO_2\uparrow$ and $Sc_2CO_2\downarrow$, respectively. As shown in Fig. 1d and a Pd single-atom anchored on the upper surface of $Sc_2CO_2\uparrow$ (denoted as Pd@$Sc_2CO_2\uparrow$) locates in the hollow site, facing the C atom below. The calculated binding energy is −1.94 eV. Since the upper surface of $Sc_2CO_2\uparrow$ is enriched with photogenerated holes, this facilitates the migration of photogenerated holes to the Pd atom supported on this surface. To enable the Pd atom to truly capture photogenerated holes, the electronic structure of the system requires that the intermediate state introduced by Pd in the bandgap is an occupied state close to the VBM (Fig. 1b). When the polarization direction of Sc_2CO_2 is reversed (Fig. 1e), the Pd atom is preferentially anchored at the bridge site on the upper surface of $Sc_2CO_2\downarrow$ (denoted as Pd@$Sc_2CO_2\downarrow$), with a binding energy of −1.24 eV. The upper surface of $Sc_2CO_2\downarrow$ is enriched with photogenerated electrons, leading the Pd atom of Pd@$Sc_2CO_2\downarrow$ to tend to accept photogenerated electrons. Accordingly, to facilitate the true capture of photogenerated electrons by the Pd atom, the intermediate state introduced by Pd in the bandgap should be an empty state close to the CBM (Fig. 1c). We qualitatively demonstrated the possibility of capturing photogenerated electrons or holes by a Pd single-atom anchored on the same surface of Sc_2CO_2 with different polarization directions, as well as the electronic structure properties needed to truly realize the capture.

To ensure the stability of the Pd atom anchored on the surface of Sc_2CO_2 with different polarization directions, AIMD simulations were conducted at 500 K for 9 ps. As shown in Fig. 2a and b, the energy fluctuations for both Pd@$Sc_2CO_2\uparrow$ and Pd@$Sc_2CO_2\downarrow$ remain within a reasonable range. The final configurations resulting from the AIMD simulations are also presented in Fig. 2a and b. It is suggested that, regardless of the polarization direction of Sc_2CO_2, the Pd atom remains the corresponding adsorption structure after being subjected to a temperature of 500 K for 9 ps. The Pd atom remains coordinated at the hollow site or bridge site without evident diffusion or detachment (Fig. S1), implying the stability of Pd atom anchoring. Photostability is a critical consideration in the evaluation of photocatalysts. Previous studies have shown that fragile, localized lone-pair contributions from anions at the VBM render anionic components susceptible to oxidation. In contrast, strong metal-anion hybridization at the VBM can substantially reduce the thermodynamic driving force and lower the likelihood of direct oxidation of lattice atoms by photogenerated holes.[41] Thus, the projected density of states (PDOS) of Sc_2CO_2 (Fig. S2) was calculated. The PDOS of Sc_2CO_2 reveals that the VBM originates from strong hybridization among Sc-3d, C-2p, and O-2p orbitals, indicating that the C and O atoms are resistant to oxidation by photogenerated holes. Moreover, prior investigations on structurally analogous MXene materials, such as Ti_2CO_2,[42] have demonstrated good photostability. On this basis, it is inferred that Sc_2CO_2 also exhibits favorable photostability.

To demonstrate that a Pd atom can indeed capture photogenerated holes or electrons, the electronic properties of Pd@$Sc_2CO_2\uparrow$ and Pd@$Sc_2CO_2\downarrow$ are analyzed. Both Pd@$Sc_2CO_2\uparrow$ and Pd@$Sc_2CO_2\downarrow$ exhibit direct band gaps, with the VBM and CBM located at the Γ point (Fig. 2c and d). The band structure associated with the band edge arrangement of the Sc_2CO_2 monolayer is shown in Fig. S3, which is consistent with previous research.[40] Compared to the band structure of the Sc_2CO_2 monolayer, an intermediate band is introduced within the original band gap of Sc_2CO_2 in both Pd@$Sc_2CO_2\uparrow$ and Pd@$Sc_2CO_2\downarrow$. The intermediate band of Pd@$Sc_2CO_2\uparrow$ is a fully occupied band lying above the VBM of the original Sc_2CO_2, while the intermediate band of Pd@$Sc_2CO_2\downarrow$ is an empty band lying below the CBM of the original Sc_2CO_2. Due to the presence of these intermediate bands, the band gaps of Pd@$Sc_2CO_2\uparrow$ and

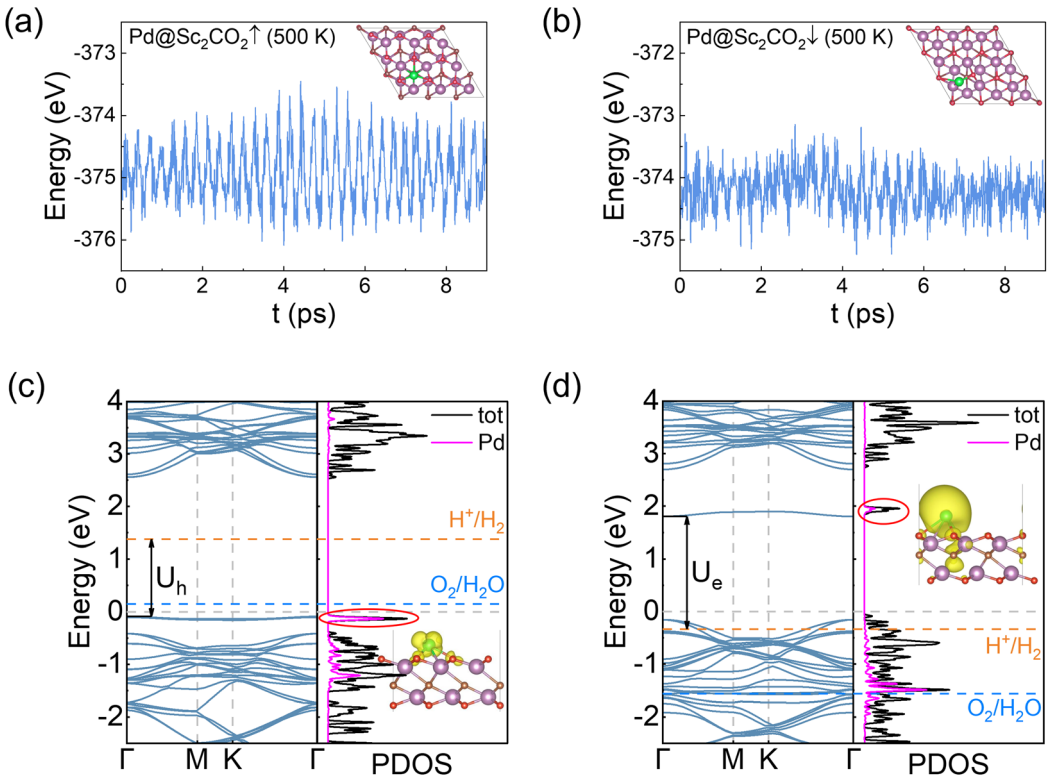

Fig. 2 Energy fluctuations for the AIMD simulations at a temperature of 500 K for (a) Pd@Sc_2CO_2↑, (b) Pd@Sc_2CO_2↓. The insets present geometric structures of Pd@Sc_2CO_2 after AIMD simulations. Band structure (left) and PDOS (right) of (c) Pd@Sc_2CO_2↑, (d) Pd@Sc_2CO_2↓. The black line shows the total DOS varies with energy, and the magenta line represents the projected DOS on the Pd atom. The red dotted circle outlines the Pd-contributed intermediate state, and the corresponding distribution of charge density in real space is shown in insets. The orange and blue dashed lines denote the potential of H^+/H_2 and O_2/H_2O for the Pd anchored surfaces. The gray dashed lines denote the Fermi levels.

Pd@Sc_2CO_2↓ are reduced from 3.02 eV to 2.64 eV and 1.96 eV, respectively, which is beneficial for enhancing light absorption. To further identify the contribution of different atoms to the intermediate bands of Pd@Sc_2CO_2↑ and Pd@Sc_2CO_2↓, the PDOS of the Pd atom is calculated (Fig. 2c and d). The results indicate that the intermediate bands of both Pd@Sc_2CO_2↑ and Pd@Sc_2CO_2↓ are primarily contributed by the Pd atom. The conclusion is also supported by the distribution of charge density for the intermediate bands in real space (insets in Fig. 2c and d). The electronic structures of Pd@Sc_2CO_2↑ and Pd@Sc_2CO_2↓ are consistent with the expectation illustrated in Fig. 1b and d. Moreover, the PDOS for varying concentrations of Pd single-atom evidences that the concentration of Pd single-atoms does not alter the characteristics of the intermediate states contributed by Pd within the band gap (Fig. S4).

In this study, the typical photocatalytic reduction and oxidation reactions of the HER and OER are selected as model reactions to evaluate the feasibility of Pd@Sc_2CO_2 for driving both reduction and oxidation reactions. Therefore, the potentials of H^+/H_2 and O_2/H_2O are plotted within the PDOS of the Pd atom (Fig. 2c and d) to explore the energy level arrangement between the Pd-contributed intermediate bands and the potentials of H^+/H_2 and O_2/H_2O. Due to the FE polarization of Sc_2CO_2, the electrostatic potential (Fig. S5) reveals a difference of 1.80 eV and −2.05 eV between the upper and lower surfaces for Pd@Sc_2CO_2↑ and Pd@Sc_2CO_2↓, respectively. After supporting the Pd atom, the change in the dipole moment of Sc_2CO_2 is modest, remaining within 10% (Table S1). These differences result in a distinct energy level arrangement between the Pd-contributed intermediate states and potentials of H^+/H_2 and O_2/H_2O. For Pd@Sc_2CO_2↑, the potential of O_2/H_2O lies above the Pd-contributed intermediate band, indicating that photogenerated holes at the Pd site can drive the OER. For Pd@Sc_2CO_2↓, the potential of H^+/H_2 lies below the Pd-contributed intermediate band, evidencing that photogenerated electrons at the Pd site can drive the HER. The external potentials for photogenerated holes (U_h) and electrons (U_e) to drive the OER and HER, respectively, are calculated by the formulae: $U_h = E(H^+/H_2) - E(\mathrm{VBM})$ and $U_e = E(\mathrm{CBM}) - E(H^+/H_2)$, where $E(H^+/H_2)$, $E(\mathrm{VBM})$, and $E(\mathrm{CBM})$ are the potential of H^+/H_2, VBM, and CBM. For Pd@Sc_2CO_2↑, the potentials of H^+/H_2 and VBM are determined to be 1.38 and −0.09 eV, respectively, providing an external potential of U_h = 1.47 V for photogenerated holes to drive the OER at the Pd site. For Pd@Sc_2CO_2↓, the potentials of H^+/H_2 and VBM are located at −0.33 and 1.88 eV, respectively, offering an external potential of U_e = 2.21 V for photogenerated electrons to drive the HER at the Pd site.

The effective capture of photogenerated holes by the Pd atom in Pd@Sc_2CO_2↑ and photogenerated electrons by the Pd atom

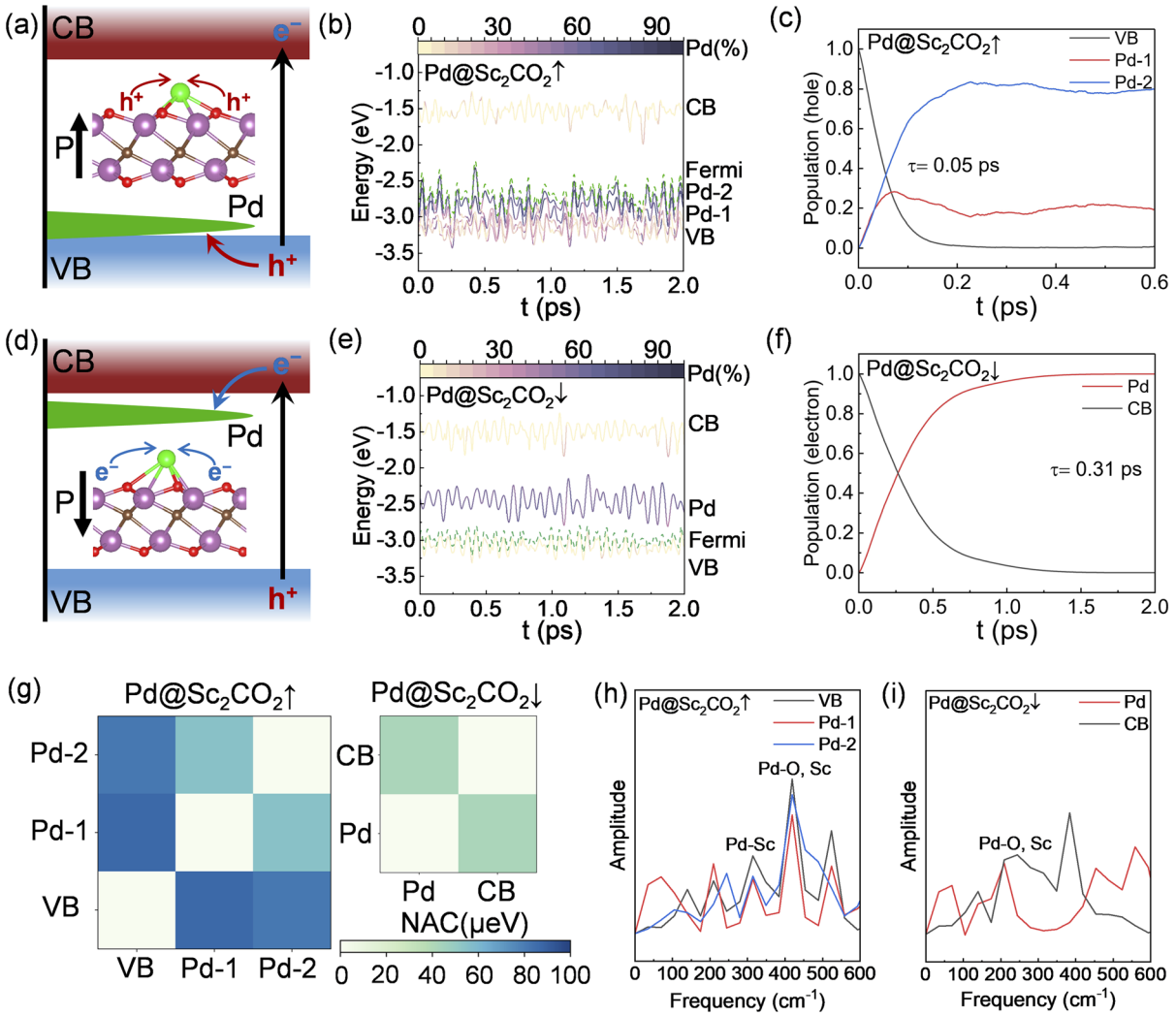

Fig. 3 Schematic diagram of migration in the energy space and real space for photogenerated (a) holes and (d) electrons. Energy fluctuations of the bands for (b) Pd@Sc_2CO_2↑ and (e) Pd@Sc_2CO_2↓. (c) Populations of holes migrating from the VB of Sc_2CO_2↑ to the Pd-contributed intermediate band in Pd@Sc_2CO_2↑. (f) Populations of electrons migrating from the CB of Sc_2CO_2↓ to the Pd-contributed intermediate band in Pd@Sc_2CO_2↓. (g) Nonadiabatic couplings (NAC) between VB, Pd-1, and Pd-2 in Pd@Sc_2CO_2↑ (left), as well as CB and Pd in Pd@Sc_2CO_2↓ (right). Fourier transforms for energy fluctuations of bands for (h) Pd@Sc_2CO_2↑ and (i) Pd@Sc_2CO_2↓.

in Pd@Sc_2CO_2↓ is qualitatively demonstrated by the analysis of electronic structures. NAMD simulations are conducted to determine whether photogenerated holes or electrons indeed migrate to the Pd atom in Pd@Sc_2CO_2↑ or Pd@Sc_2CO_2↓. To obtain trajectories for NAMD simulations, AIMD simulations at 300 K for 9 ps with NVT and NVE ensembles are performed (Fig. S6). Fig. 3a and d show the schematic diagram of migration in the energy space and real space for photogenerated holes and electrons, respectively. The time-dependent energy fluctuations of the bands in Pd@Sc_2CO_2↑ and Pd@Sc_2CO_2↓ during a 2 ps MD simulation at 300 K are shown in Fig. 3b and e, respectively. Two intermediate states between the valence band (VB) and the Fermi level, primarily contributed by the Pd atom (denoted as Pd-1 and Pd-2), are identified for trapping holes in Pd@Sc_2CO_2↑. These Pd states are close to the VB and Fermi level in energy but do not cross the VB or Fermi level. In contrast, one Pd-contributed intermediate state between the conduction band (CB) and the Fermi level is demonstrated to trap electrons in Pd@Sc_2CO_2↓. The energy of this Pd state is stable and does not cross the CB or Fermi level. Fig. 3c and f illustrate the time-dependent population of photogenerated holes and electrons in Pd@Sc_2CO_2↑ and Pd@Sc_2CO_2↓, respectively. The time constant τ is obtained by fitting the time population of photogenerated holes or electrons with the exponential function $f(t) = \exp(-t/\tau)$. The ultrafast τ of 0.05 ps is obtained for photogenerated holes migrating from Sc_2CO_2 to Pd in Pd@Sc_2CO_2↑, while the rapid τ of 0.31 ps is fitted for photogenerated electron transfer from Sc_2CO_2 to Pd in Pd@Sc_2CO_2↓.

The migration of carriers between energy bands is influenced by nonadiabatic coupling (NAC), which is calculated using the formula:

$$d_{jk} = \left\langle \phi_j \left| \frac{\partial}{\partial t} \right| \phi_k \right\rangle = \sum_i \frac{\langle \phi_j | \nabla_{R_i} H | \phi_k \rangle}{\varepsilon_k - \varepsilon_j} \dot{R}_i$$

where H is the Kohn–Sham Hamiltonian, φ_i, φ_j, ε_j, and ε_k are the wave functions and eigenvalues of electronic states j and k, respectively, and $\dot{R}_i$ is the nuclear velocity. Therefore, NAC depends mainly on the energy difference $\varepsilon_k - \varepsilon_j$, the electron–phonon coupling term $\langle\varphi_j|\nabla_{R_i}H|\varphi_k\rangle$ and the nuclear velocity $\dot{R}_i$. A larger NAC indicates a higher probability for migration of carriers between two energy bands. The average of the absolute value of NAC between different bands of Pd@Sc_2CO_2 is shown in Fig. 3g. The NAC between the VB and Pd-1 bands in Pd@Sc_2CO_2↑ exceeds 80 μeV, while the NAC between the CB and Pd bands in Pd@Sc_2CO_2↓ exceeds 40 μeV. This shows that both photogenerated holes and electrons have the probability of migrating to the Pd atom, but holes migrate more rapidly than electrons. Fourier transform of the energy fluctuations of each energy band in Pd@Sc_2CO_2 is also calculated to identify the characteristic phonon modes (Fig. 3h and i). The frequency corresponding to each peak in the curve represents a phonon mode, which corresponds to the vibration frequency of the Pd–O or Pd–Sc bond in real space. To research this correspondence, the vibration frequencies of the Pd–O and Pd–Sc bonds in the Pd@Sc_2CO_2 system are calculated (Table S2). The overlap of characteristic peaks of different energy bands indicates potential channels for carrier migration between energy bands. For Pd@Sc_2CO_2↑ (Fig. 3g), the characteristic peaks of Pd-1 and VB overlap around 209 cm^{-1}, corresponding to the rocking vibration frequency of Sc–Pd–O. The overlapping peaks of Pd-1, Pd-2, and VB near 419 cm^{-1} are likely associated with the stretching vibration of the Pd–O bond. This suggests that photogenerated holes migrate from Sc_2CO_2 to the Pd atom through the vibration of the Pd–O bond. For Pd@Sc_2CO_2↓ (Fig. 3h), the characteristic peaks for Pd and CB overlap around 209 cm^{-1}, which can be interpreted as the stretching vibration of the Pd–Sc bond. This indicates that photogenerated electrons migrate from Sc_2CO_2 to the Pd atom *via* the vibration of the Pd–Sc bond. On the one hand, photogenerated hole transfer to the Pd atom is faster than electron transfer due to the larger NAC and the smaller energy gap. On the other hand, the results of NAMD confirm that both carriers migrate to the Pd atom within tens to hundreds of femtoseconds, significantly faster than the reverse migration of carriers from the Pd atom to Sc_2CO_2 (Fig. S7), validating the proposed strategy of modulating migration dynamics for carriers by switching out-of-plane polarization. Therefore, it is actionable to selectively accumulate either electrons or holes on the Pd atom.

To switch the photocatalytic reactions between oxidation and reduction, the photogenerated holes or electrons in Sc_2CO_2 not only migrate separately to the Pd atom, but also participate in the oxidation or reduction reaction at the Pd active site. The exploration of the band edge arrangement has qualitatively demonstrated the feasibility of Pd@Sc_2CO_2↑ for driving the OER and Pd@Sc_2CO_2↑ for driving the HER. In the following, we will discuss the mechanism of the OER and HER. The reaction pathways of four-electron OER are complex, involving three intermediates: *OH, *O, and *OOH. The reaction pathway and free energy profile of the OER proceeding at the Pd site of Pd@Sc_2CO_2↑ under neutral conditions (pH = 7) are illustrated in Fig. 4a, while the results under acidic (pH = 0) and alkaline

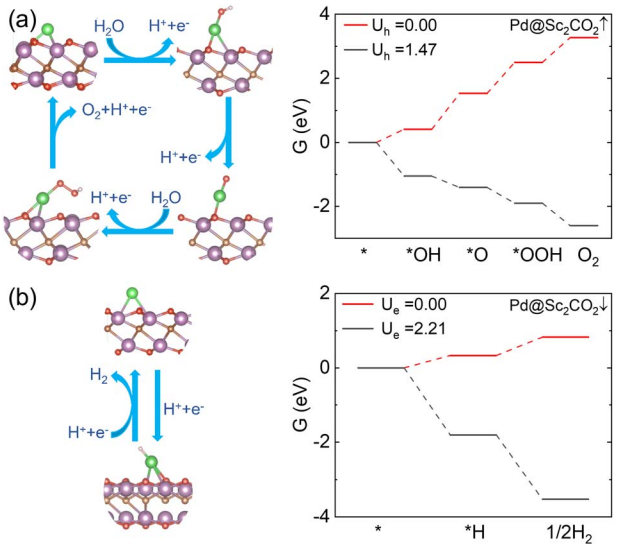

Fig. 4 Proposed photocatalytic pathway (left) and corresponding free-energy change (right) of (a) the OER at the Pd atom site in Pd@Sc_2CO_2↑ and (b) HER at the Pd atom site in Pd@Sc_2CO_2↓ under the condition of pH = 7.

(pH = 14) conditions are presented in Fig. S5. The results reveal that the OER at the Pd site of Pd@Sc_2CO_2↑ proceeds with an overpotential η of 0.29 V. The potential-determining step is identified as *OH → *O + H^+ + e^-. After taking the external potential provided by photogenerated holes (U_h = 1.47 V), all elementary reactions of the OER proceed spontaneously. In contrast, the reaction pathway and free energy profile of the HER proceeding at the Pd site of Pd@Sc_2CO_2 ↓ at pH = 7 are shown in Fig. 4b, with a predicted overpotential η of 0.08 V. Owing to the high external potential provided by photogenerated electrons (U_e = 2.21 V), the HER can spontaneously proceed. Since the oxidation reaction involves the step of losing protons and electrons, while the reduction reaction involves gaining electrons, a higher pH value favors the oxidation reaction but hinders the reduction reaction. The OER and HER can spontaneously proceed under both acidic (pH = 0) and alkaline (pH = 14) conditions at the Pd site of Pd@Sc_2CO_2↑ and Pd@Sc_2CO_2↓, respectively, with the external potential provided by photogenerated carriers (Fig. S8). Moreover, the sensitivity of the reaction free energy changes to solvation effects[43] and the loading concentration of single-atoms is assessed to confirm the robustness of the reaction thermodynamics for water splitting (Fig. S9). The resulting profiles exhibit qualitatively similar trends to those obtained from gas-phase calculations employing a 3 × 3 supercell. Consequently, it is demonstrated that the Pd atom anchored on the upper surface of Sc_2CO_2↑ drives the photocatalytic oxidation reaction, while the Pd atom anchored on the same surface of Sc_2CO_2↓ drives the photocatalytic reduction reaction.

The above results confirm the viability of the proposed strategy. Nevertheless, it should be pointed out that the models of surface-anchored Pd single atoms presented here are constructed under idealized assumptions. Under realistic catalytic conditions, the retention of the ability of Pd single atoms to

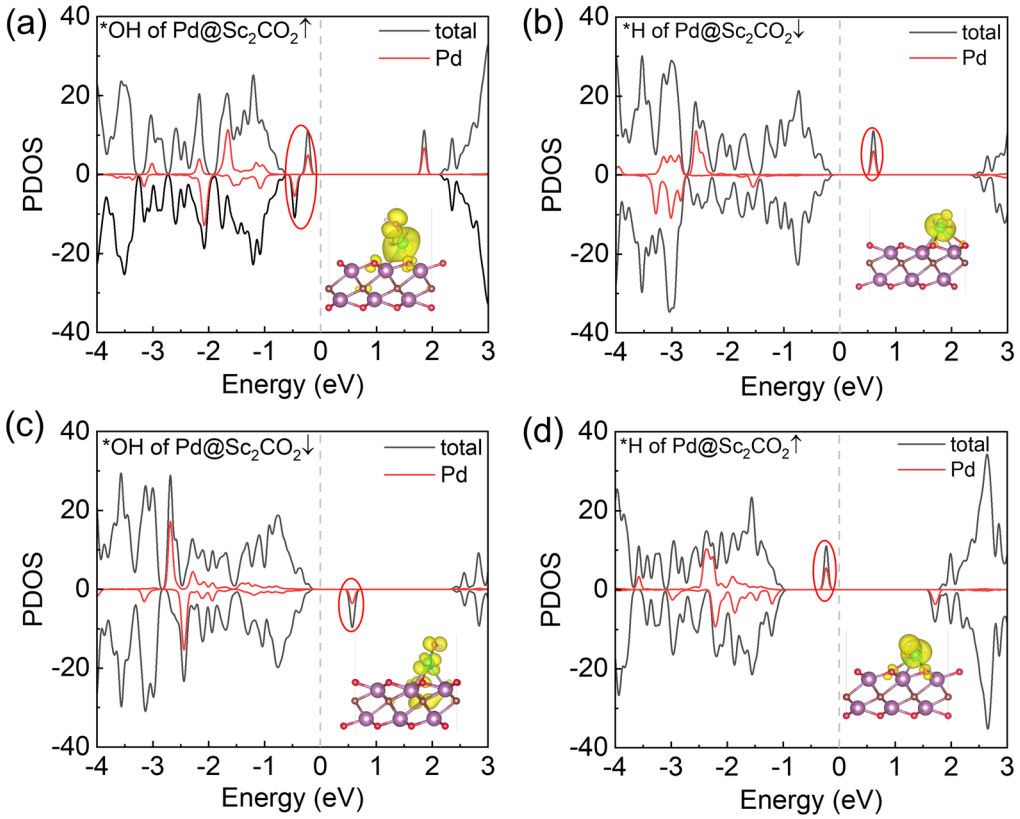

Fig. 5 The PDOS for adsorbed species: (a) *OH of Pd@Sc_2CO_2↑, (b) *H of Pd@Sc_2CO_2↓, (c) *OH of Pd@Sc_2CO_2↓, and (d) *H of Pd@Sc_2CO_2↑. The red circle outlines the Pd-contributed intermediate state, and the corresponding distribution of charge density in real space is shown in the inset.

selectively capture photogenerated holes and electrons across different FE polarization orientations of Sc_2CO_2, even after the adsorption of reaction intermediates, serves as a key metric for evaluating the operational durability of Pd@Sc_2CO_2. In particular, the removal of residual intermediates from Pd sites following FE polarization switching is critical to preventing the deactivation of the Pd single atoms. Reaction pathway analyses reveal that *H and *OH are the most persistent intermediates during the HER and OER, respectively. Accordingly, we examined the electronic structure characteristics of *H and *OH adsorbates under varying FE polarization directions. Fig. 5a and b present the PDOS of Pd with adsorbed *OH and *H under reaction conditions. In the case of *OH-adsorbed Pd@Sc_2CO_2↑, the Pd-contributed intermediate states remain occupied above the VB. By contrast, for *H-adsorbed Pd@Sc_2CO_2↓, the Pd-derived intermediate states appear as unoccupied states within the band gap. This electronic behavior aligns with that observed for Pd in the absence of adsorbates, demonstrating that the presence of adsorbates does not compromise the capacity of Pd to selectively capture photogenerated electrons and holes. Following FE polarization reversal in Sc_2CO_2, residual *OH or *H species may persist on Pd atoms, thereby influencing their catalytic performance in subsequent redox reactions. For example, Pd sites originally facilitating the HER may retain *H, which can suppress their OER activity; conversely, those involved in the OER may retain *OH, impairing their HER performance. To investigate the regeneration mechanism, we computed the PDOS of Pd with residual *OH or *H adsorbates after polarization switching (Fig. 5c and d). For *OH-residual Pd@Sc_2CO_2↓, the Pd-induced states are unoccupied within the band gap, indicating that Pd can capture photogenerated electrons to reduce residual *OH to H_2O or desorb it as OH^-, thereby recovering catalytic activity. In the case of *H-residual Pd@Sc_2CO_2↑, the Pd-derived states remain occupied above the VB, suggesting that photogenerated holes can be captured to oxidize residual *H to H_2O or release it as H^+, thus restoring catalytic function.

In this study, the 2D FE material Sc_2CO_2, characterized by its out-of-plane polarization, was employed as a substrate for anchoring SACs to assess the feasibility of our proposed strategy. Central to this approach is the modulation of the energetic positions of the single-atom intermediate states within the band gap *via* FE polarization switching, which enables the distinct capture of photogenerated electrons and holes under different polarization orientations. Beyond Sc_2CO_2, a variety of experimentally synthesized 2D materials exhibiting out-of-plane ferroelectricity, including In_2Se_3,[29] $CuInP_2S_6$,[44] and $AgBiP_2Se_6$,[45] have also been documented. Moreover, in certain bilayer systems such as WTe_2,[46] BN,[47] and InSe,[48] switching of the out-of-plane polarization can be induced by interlayer sliding.[49] The integration of such FE substrates with appropriately selected single atoms offers a promising pathway for

designing a wide range of single-atom photocatalysts exhibiting similar reaction-switching properties. Moreover, the proposed strategy can be extended to other photocatalytic transformations. As an illustrative example, in the widely investigated homocoupling of methane to ethane,[50,51] the reduction half-reaction is the HER, while the oxidation half-reaction is the ethane evolution reaction. The switching of the FE polarization direction leads to the accumulation of either photogenerated electrons or holes on the Pd atom, thereby enabling the Pd active site to drive either the HER or the ethane evolution reaction. The reaction pathway for the HER on the Pd site of Pd@Sc_2CO_2↓ is the same as that in water splitting (Fig. 4b). The overpotential for the ethane evolution reaction on the Pd site of Pd@Sc_2CO_2↑ is as low as 0.45 V, and the Pd active sites easily drive this reaction by leveraging the energy supplied by photogenerated holes (Fig. S10). Identical to water splitting, the free energy changes show similar trends compared to the 3×3 supercell model in the gas phase and overall spontaneity after the consideration of solvation effects and loading concentration of the single atom (Fig. S10). Moreover, the potential competition from overoxidation is also evaluated. It is found that the competition from overoxidation exhibits weak competitiveness compared to the desired methane coupling (Fig. S11). The results highlight the potential of our approach across a spectrum of redox processes.

Conclusions

In summary, our theoretical study proposes the FE photocatalyst Pd@Sc_2CO_2 for redox reaction switching at a single active site through polarization-induced reversible electron–hole migration. By leveraging the reversible out-of-plane polarization of the FE Sc_2CO_2 substrate, we demonstrate dynamically controlled migration of photogenerated electrons or holes to the Pd single-atom site anchored on the upper surface of Sc_2CO_2, enabling the switch between photocatalytic reduction and oxidation reactions. Crucially, Pd anchoring creates distinct intermediate states within the band gap of Sc_2CO_2: upward polarization yields an occupied Pd state near the VBM, facilitating ultrafast hole capture ($\tau = 0.05$ ps), while downward polarization generates an empty Pd state near the CBM, enabling rapid electron capture ($\tau = 0.31$ ps). Free energy profiles confirm the spontaneous thermodynamics for both the HER and OER at the Pd site when driven by the corresponding photogenerated carriers. Notably, our study demonstrates from both thermodynamic and kinetic perspectives that flipping the polarization direction of Sc_2CO_2 dynamically controls electrons or holes migrating to the Pd active site, thereby switching its photocatalytic function between reduction and oxidation reactions. This strategy provides a novel design principle for SACs capable of driving and switching between distinct photocatalytic reactions.

Author contributions

C. Fu and X. Li conceived the idea for this study and designed the research. Y. Tang conducted the research. Y. Tang wrote the manuscript and all authors assisted with editing, analysis, and interpretation.

Conflicts of interest

There are no conflicts to declare.

Data availability

The data supporting this article have been included as part of the supplementary information (SI). Supplementary information: computational method, mechanism of the OER and HER, band structures of the Sc_2CO_2 monolayer, geometric structure and band structure of Sc_2CO_2, PDOS of Pd@Sc_2CO_2↑ and Pd@Sc_2CO_2↓ with $2 \times 2 \times 1$ and $4 \times 4 \times 1$ supercells of monolayer Sc_2CO_2, electrostatic potential along the perpendicular direction of Pd@Sc_2CO_2↑ and Pd@Sc_2CO_2↓, results of AIMD under NVT and NVE conditions at 300 K, recombination time of the photogenerated carriers, free energy change under acidic and alkaline conditions for the OER on Pd@Sc_2CO_2↑ and HER on Pd@Sc_2CO_2↓, free-energy change for the ethane evolution reaction, the dipole moment of Sc_2CO_2, Pd@Sc_2CO_2↑ and Pd@Sc_2CO_2↓, frequency for vibration of the Pd–O, Pd–Sc bond and characteristic peak. See DOI: https://doi.org/10.1039/d5sc09491g.

Acknowledgements

This work was partially supported by the National Natural Science Foundation of China (22273092, 22073085 and 22322304), the Innovation Program for Quantum Science and Technology (2021ZD0303306), the Strategic Priority Research Program of the Chinese Academy of Sciences (XDB0450101), and the USTC Tang Scholar. The numerical calculations have been done on the supercomputing system in the USTC-SCC.

References

1 W. Wang, H. Zhang, S. Zhang, Y. Liu, G. Wang, C. Sun and H. Zhao, *Angew. Chem., Int. Ed.*, 2019, **58**, 16644–16650.
2 X. Liu, Y. Li, J. Zhang and J. Lu, *Nano Res.*, 2021, **14**, 3372–3378.
3 X. X. Li, Z. Y. Li and J. L. Yang, *Phys. Rev. Lett.*, 2014, **112**, 018301.
4 S. Fang and Y. H. Hu, *Chem. Soc. Rev.*, 2022, **51**, 3609–3647.
5 W. Chi, Y. Dong, B. Liu, C. Pan, J. Zhang, H. Zhao, Y. Zhu and Z. Liu, *Nat. Commun.*, 2024, **15**, 5316.
6 Y. Li, J. Li, W. Yang and X. Wang, *Nanoscale Horiz.*, 2020, **5**, 1174–1187.
7 W. Shang, Y. Li, H. Huang, F. Lai, M. B. J. Roeffaers and B. Weng, *ACS Catal.*, 2021, **11**, 4613–4632.
8 L. Quan, H. Jiang, G. Mei, Y. Sun and B. You, *Chem. Rev.*, 2024, **124**, 3694–3812.
9 X. Wu, C. Tang, Y. Cheng, X. Min, S. P. Jiang and S. Wang, *Chem.–Eur. J.*, 2020, **26**, 3906–3929.
10 S. Ali, P. M. Ismail, M. Khan, A. Dang, S. Ali, A. Zada, F. Raziq, I. Khan, M. S. Khan, M. Ateeq, W. Khan, S. H. Bakhtiar, H. Ali, X. Wu, M. I. A. Shah, A. Vinu, J. Yi, P. Xia and L. Qiao, *Nanoscale*, 2024, **16**, 4352–4377.

11 K. R. G. Lim, A. D. Handoko, S. K. Nemani, B. Wyatt, H.-Y. Jiang, J. Tang, B. Anasori and Z. W. Seh, *ACS Nano*, 2020, **14**, 10834–10864.
12 G. Murali, J. K. Reddy Modigunta, Y. H. Park, J.-H. Lee, J. Rawal, S.-Y. Lee, I. In and S.-J. Park, *ACS Nano*, 2022, **16**, 13370–13429.
13 L. Ju, M. Bie, X. Tang, J. Shang and L. Kou, *ACS Appl. Mater. Interfaces*, 2020, **12**, 29335–29343.
14 J. Xiao, X. Liu, L. Pan, C. Shi, X. Zhang and J.-J. Zou, *ACS Catal.*, 2020, **10**, 12256–12283.
15 L. Liu and H. Huang, *Chem.–Eur. J.*, 2022, **28**, e202103975.
16 T. L. Wan, L. Ge, Y. Pan, Q. Yuan, L. Liu, S. Sarina and L. Kou, *Nanoscale*, 2021, **13**, 7096–7107.
17 A. Kakekhani and S. Ismail-Beigi, *J. Mater. Chem. A*, 2016, **4**, 5235–5246.
18 H. Liu, S. Yu, Y. Wang, B. Huang, Y. Dai and W. Wei, *J. Phys. Chem. Lett.*, 2022, **13**, 1972–1978.
19 A. Kakekhani and S. Ismail-Beigi, *ACS Catal.*, 2015, **5**, 4537–4545.
20 M. Cheng, Y. Si, N. Li and J. Guan, *J. Am. Chem. Soc.*, 2024, **146**, 26567–26573.
21 C.-H. Chiang, C.-C. Lin, Y.-C. Lin, C.-Y. Huang, C.-H. Lin, Y.-J. Chen, T.-R. Ko, H.-L. Wu, W.-Y. Tzeng, S.-Z. Ho, Y.-C. Chen, C.-H. Ho, C.-J. Yang, Z.-W. Cyue, C.-L. Dong, C.-W. Luo, C.-C. Chen and C.-W. Chen, *J. Am. Chem. Soc.*, 2024, **146**, 23278–23288.
22 X. Jiang, J. Tan, D. Liu, Y. Feng, K.-Q. Chen, E. A. Kazakova, A. S. Vasenko and E. V. Chulkov, *J. Phys. Chem. Lett.*, 2024, **15**, 3611–3618.
23 L. Ju, Y. Ma, X. Tan and L. Kou, *J. Am. Chem. Soc.*, 2023, **145**, 26393–26402.
24 L. Ju, J. Shang, X. Tang and L. Kou, *J. Am. Chem. Soc.*, 2019, **142**, 1492–1500.
25 L. Ju, X. Tan, X. Mao, Y. Gu, S. Smith, A. Du, Z. Chen, C. Chen and L. Kou, *Nat. Commun.*, 2021, **12**, 5128.
26 H. Ma, X. Ye, X. Li, Z. J. Xu and Y. Sun, *Adv. Mater.*, 2025, **37**, 2500285.
27 C. Rong, T. Su, Z. Li, T. Chu, M. Zhu, Y. Yan, B. Zhang and F.-Z. Xuan, *Nat. Commun.*, 2024, **15**, 1566.
28 A. Chandrasekaran, A. Mishra and A. K. Singh, *Nano Lett.*, 2017, **17**, 3290–3296.
29 Y. Zhou, D. Wu, Y. Zhu, Y. Cho, Q. He, X. Yang, K. Herrera, Z. Chu, Y. Han, M. C. Downer, H. Peng and K. Lai, *Nano Lett.*, 2017, **17**, 5508–5513.
30 Z.-Z. Sun, W. Xun, L. Jiang, J.-L. Zhong and Y.-Z. Wu, *J. Phys. D: Appl. Phys.*, 2019, **52**, 465302.
31 Y. Fan, X. Song, H. Ai, W. Li and M. Zhao, *ACS Appl. Mater. Interfaces*, 2021, **13**, 34486–34494.
32 F. Wang, L. Ju, B. Wu, S. Li, J. Peng, Y. Chen, M. Getaye Sendeku, K. Wang, Y. Cai, J. Yi, Y. Yang, Z. Wang and X. Sun, *Angew. Chem., Int. Ed.*, 2024, **63**, e202402033.
33 T. Zhang, X. Niu, Q. Chen, J. Wang and J. Phy, *Chem. Lett.*, 2025, **16**, 675–681.
34 W. Li, H. Zhang, R. Xu, X. Jiang, H. Meng, X.-X. Xue and S. Zhang, *Chem. Eng. J.*, 2025, **505**, 159247.
35 J. Wang, J. Lu, X. Zhao, G. Hu, X. Yuan, J. Ren and S. Qi, *J. Catal.*, 2026, **454**, 116664.
36 F. Seidi, A. Arabi Shamsabadi, M. Dadashi Firouzjaei, M. Elliott, M. R. Saeb, Y. Huang, C. Li, H. Xiao and B. Anasori, *Small*, 2023, **19**, 2206716.
37 M. Naguib, M. Kurtoglu, V. Presser, J. Lu, J. Niu, M. Heon, L. Hultman, Y. Gogotsi and M. W. Barsoum, *Adv. Mater.*, 2011, **23**, 4248–4253.
38 M. Naguib, V. N. Mochalin, M. W. Barsoum and Y. Gogotsi, *Adv. Mater.*, 2013, **26**, 992–1005.
39 M. Khazaei, A. Ranjbar, M. Arai, T. Sasaki and S. Yunoki, *J. Mater. Chem. C*, 2017, **5**, 2488–2503.
40 C.-F. Fu, X. Li, Q. Luo and J. Yang, *J. Mater. Chem. A*, 2017, **5**, 24972–24980.
41 A. Miyoshi and K. Maeda, *Sol. RRL*, 2020, **5**, 202000521.
42 C.-F. Fu, X. Li and J. Yang, *Chem. Sci.*, 2021, **12**, 2863–2869.
43 K. Mathew, R. Sundararaman, K. Letchworth-Weaver, T. A. Arias and R. G. Hennig, *J. Chem. Phys.*, 2014, **140**, 084106.
44 C. Guo, J. Zhu, X. Liang, C. Wen, J. Xie, C. Gu and W. Hu, *Nat. Commun.*, 2024, **15**, 10152.
45 W. He, D. Wu, L. Kong, P. Yu and G. Yang, *Adv. Mater.*, 2024, **36**, 2312541.
46 Z. Fei, W. Zhao, T. A. Palomaki, B. Sun, M. K. Miller, Z. Zhao, J. Yan, X. Xu and D. H. Cobden, *Nature*, 2018, **560**, 336–339.
47 K. Yasuda, X. R. Wang, K. Watanabe, T. Taniguchi and P. Jarillo-Herrero, *Science*, 2021, **372**, 1458–1462.
48 H. Hu, Y. Sun, M. Chai, D. Xie, J. Ma and H. Zhu, *Appl. Phys. Lett.*, 2019, **114**, 252903.
49 M. Wu and J. Li, *Proc. Natl. Acad. Sci. U. S. A.*, 2021, **118**, e2115703118.
50 T. Hibino, K. Kobayashi, M. Nagao, D. Zhou, S. Chen and Y. Yamamoto, *ACS Catal.*, 2023, **13**, 8890–8901.
51 F. Amano, A. Shintani, K. Tsurui, H. Mukohara, T. Ohno and S. Takenaka, *ACS Energy Lett.*, 2019, **4**, 502–507.